JOURNAL OF MATERIALS SCIENCE 26 (1991) 5595–5607

Dissolution slowness surfaces of cubic crystals

Part II *Applications to class 23 and to combined etching and lithography techniques*

C. R. TELLIER, J. Y. AMAUDRUT, A. BRAHIM-BOUNAB
Laboratoire de Chronométrie, Electronique et Piézoélectricité, Ecole Nationale Superieure de Mecanique et des Microtechniques, Route de Gray, La Bouloie, 25030 Besancon Cedex, France

Procedures are developed to derive the etching shapes encountered in conventional crystal etching and in localized crystal dissolution. These procedures are used to predict the shapes produced on class 23 crystals. Problems of practical importance in photolithography techniques, such as the extent of the underetch, the bordering angle and the etched shape of star-like structures, are studied. In some cases the results are compared with those obtained from geometrical constructions based on Wulff's procedure.

1. Introduction

Over the past few years, the prediction of etching shapes such as hillocks and pit formation [1–6], and of limiting shapes for starting cylindrical hollows or cylindrical crystals [7, 8] has often been based on the two criteria stated by Batterman [9–11], and later on the kinematic model of dissolution proposed by Frank [12, 13]. The Frank model in particular gives us the necessary tools to construct geometrically the etching shapes encountered in localized growth [14, 15], i.e. at the edge of an inert mask. Such constructions resemble Wulff's plots [16] and require experiments on differently oriented wafers to estimate with sufficient accuracy the polar plot corresponding to a cross-section of given orientation.

Recently, new theoretical concepts have been developed for deriving analytical expressions of the dissolution slowness surface using a tensorial representation of anisotropic etching [17–21]. In Part I of this work [21] calculations are performed for all cubic classes and applied to class 23, and emphasis has been placed on the selection of the higher rank to obtain slowness surfaces with complex shapes. In Part II, we develop new procedures to analyse the dissolution shapes of crystals and the cross-sectional shapes resulting from etching processes at mask edges. Since the trajectory of a surface element of given orientation can be derived from the equation of the slowness surface [22], all the procedures start with the analytical expression of the slowness surface.

It is also of interest to compare the geometrical procedures with the present method. The construction method, as well as the new procedure, is applied to various etching situations. We also examine simple configurations and end by studying complex structures such as star-like structures [23, 24]. Except in one section, all the graphical simulations presented in this work refer to polar diagrams of the dissolution slowness illustrated in Part I [21].

2. Dissolution shapes of starting circular sections

In this section we deal with the etched shapes of differently orientated sections when we start with a cylindrical hollow, or conversely with a cylindrical crystal. For a planar section whose orientation is defined by the angles $\varphi = \varphi_0 + 90°$, $\theta = 0°$, these shapes can be determined from the polar graph of $\mathbf{L}(\varphi_0, \theta)$ involving varying values of the angle θ. Since the polar graph presents a series of maxima and minima, the final shape of the etched section can be crudely constructed from the polar graph of $\mathbf{L}$ using the reciprocity condition for etching proposed by Irving [10]. A concave intersection formed by two initial planes is stable provided there is no plane between them with a smaller normal etch rate; conversely, a convex intersection remains stable when there is no plane between them with a higher etch rate When these conditions are not met the dissolution causes the development of curved portions of etched profiles. When we are concerned with initially circular sections we can conveniently restate the stability criteria as follows.

1. For concave intersections, i.e. when we start with a cylindrical hollow, the final dissolution shape is composed of limiting planes which correspond to maxima in the dissolution slowness. The rounded portions of the final dissolution shape can be attributed to the presence of minima in $|\mathbf{L}|$.

2. For convex intersections, i.e. for a starting cylindrical crystal, the development of limiting planar facets during the chemical attack can be associated with the minima in the dissolution slowness, whereas

0022–2461/91 $03.00 + .12

the curved portions can be correlated to the maxima in $|\mathbf{L}|$.

The use of the stability theorems 1 and 2 allows us to construct geometrically the approximate etched shape of an initially circular section. It is sufficient to draw the normals $\mathbf{n}(\varphi_0, \theta_e)$ to the particular elements forming the starting section, for which the dissolution slowness passes through an extremum at angle θ_e, and to retain the etch rate, R, given by $R(\varphi_0, \theta) = (|\mathbf{L}(\varphi_0, \theta)|)^{-1}$. The approximate dissolution shape is then formed by the limiting planes which are sometimes joined together by curved faces. The results of these simplified geometrical constructions involving the polar diagrams displayed in Figs 4 and 5d of Part I, [21], respectively, are given here in Figs 1 and 2.

This approximate procedure is suitable when the polar graph of $\mathbf{L}$ is obtained from experiments: in practice, when only the etch rate as a function of orientation is partially known. But as soon as the equation for the slowness surface is completely determined, better information on the exact dissolution shapes can be obtained by numerical methods. For this purpose we have developed numerical simulations for the graphical representation of the dissolution shapes of initially circular sections. The principal subroutines which are incorporated in the program are listed in Fig. 3. We observe that the angle of cut, φ_0, which is needed to work with a given polar graph is used as a fundamental input. The program then calculates the propagation vector $\mathbf{P}(\varphi_0, \theta)$ corresponding to the successive planar elements of orientation (φ_0, θ) which compose the starting circular section. In addition a test is made to distinguish between diverging and converging trajectories [12, 13, 18] and then to eliminate the etched elements which make no contribution at all to the final section. The results of the graphical simulation which are illustrated in Figs 4 and 5 can be compared with the geometrical constructions of Figs 1 and 2, firstly to be precise about the real contribution of extrema to the formation of limiting facets, and secondly to emphasize (if possible) the role played by the relative amplitude of successive minima and maxima in the extent of the curved portions and of the limiting planar facets. The following conclusions can be drawn.

1. According to theorem 1, and as we start with a cylindrical hollow of finite radius r_0, we observe that the maxima in $\mathbf{L}$ give rise to slightly curved limiting facets. The more accentuated the maximum, the more rapidly the limiting facet of the etched section becomes planar (see for example the facets in Fig. 4c associated with the maxima M_2 and M_3 as indicated in Fig. 5d of Part I [21]). Simultaneously, the extent of successive limiting facets is directly correlated with the relative amplitude of the successive maxima. In reality, as clearly evinced by Fig. 4c, the extent of a facet increases with the amplitude of the maximum provided this maximum remains pronounced (compare, for example, the development of the facets related to the maxima M_1 and M_4 in Fig. 5d of Part I [21]).

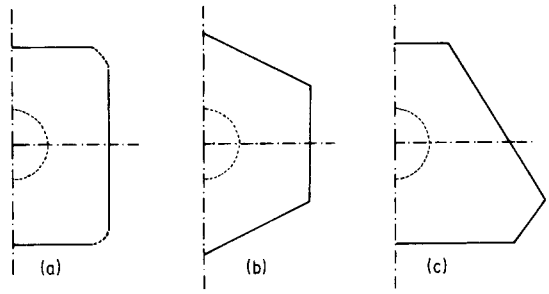

Figure 1 Theoretical dissolution shapes of a starting cylindrical hollow as estimated from geometrical constructions. (a) $N_{max} = 6$, $\varphi_0 = 0°$ (Fig. 4b, Part I [21]); (b) $N_{max} = 8$, $\varphi_0 = 0°$ (Fig. 4c, [21]); (c) $N_{max} = 10$, $\varphi_0 = 60°$ (Fig. 5d, [21]). The etched shapes are symmetrical about the vertical axis.

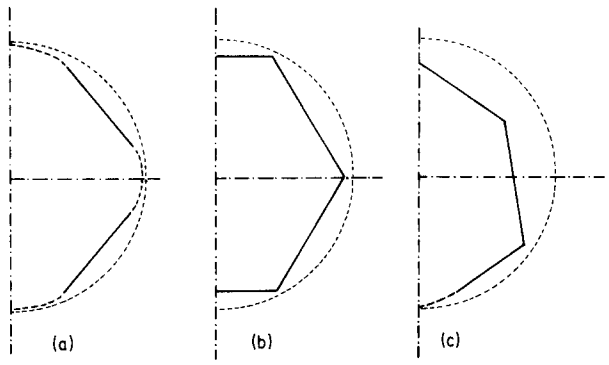

Figure 2 The theoretical dissolution shapes of a starting cylindrical crystal as estimated from geometrical constructions. (a) $N_{max} = 6$, $\varphi_0 = 0°$ (Fig. 4b, Part 1 [21]); (b) $N_{max} = 8$, $\varphi_0 = 0°$ (Fig. 4c, [21]); (c) $N_{max} = 10$, $\varphi_0 = 60°$ (Fig. 5d, [21]). The etched shapes are symmetrical about the vertical axis.

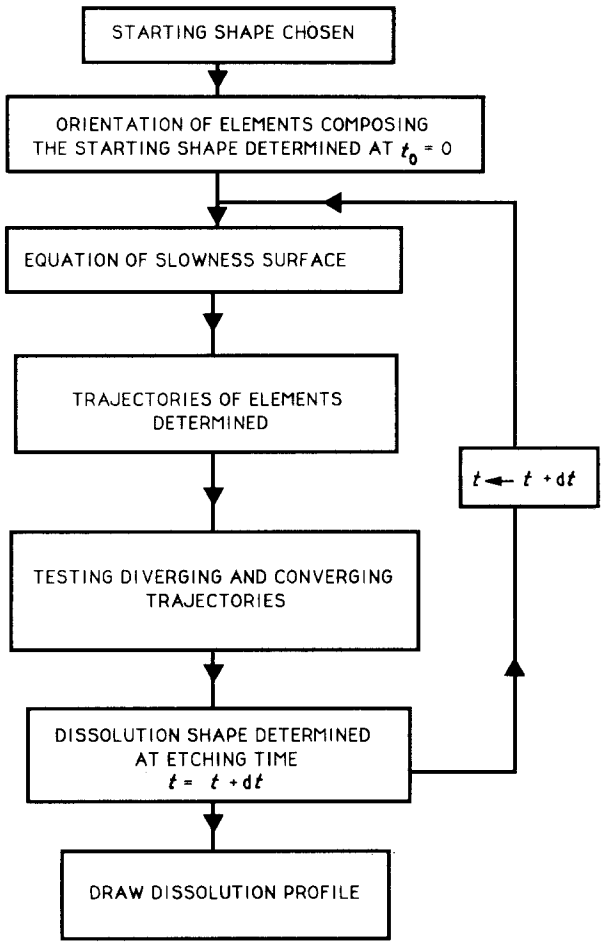

Figure 3 Flow chart of simulation.

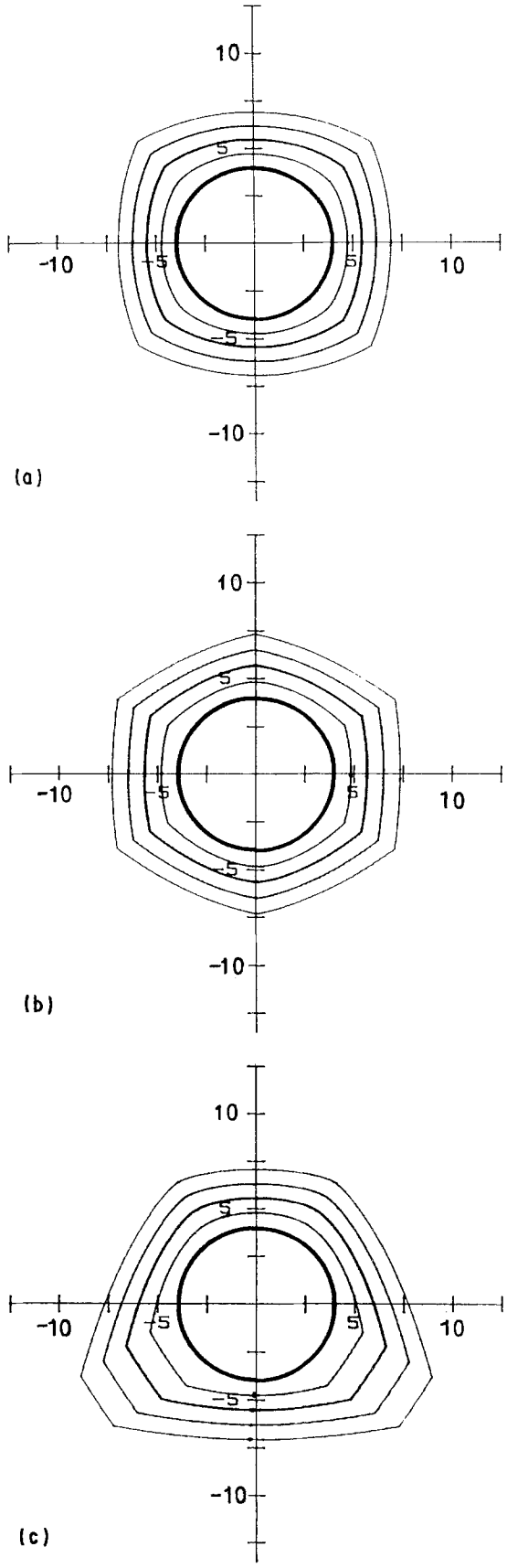

Figure 4 Graphical simulations of the dissolution shapes of a starting cylindrical hollow. (a) $N_{max} = 6$, $\varphi_0 = 0°$ (Fig. 4b, Part I [21]); (b) $N_{max} = 8$, $\varphi_0 = 0°$ (Fig. 4c, [21]); (c) $N_{max} = 10$, $\varphi_0 = 60°$ (Fig. 6, [21]).

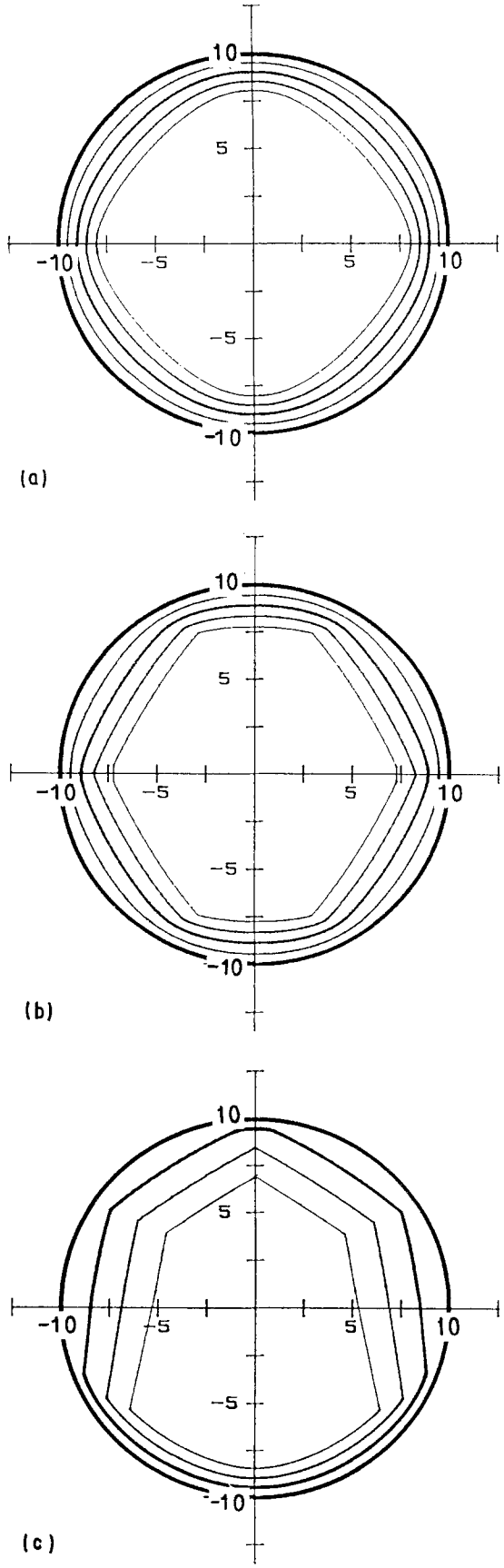

Figure 5 Graphical simulations of the dissolution shapes of a starting cylindrical crystal. (a) $N_{max} = 6$, $\varphi_0 = 0°$ (Fig. 4b, Part I [21]); (b) $N_{max} = 8$, $\varphi_0 = 0°$ (Fig. 4c, [21]); (c) $N_{max} = 10$, $\varphi_0 = 60°$ (Fig. 6, [21]).

2. For a cylindrical crystal, minima in **L** give rise to limiting facets whose extension is now determined by the amplitude of the minima. Here again, pronounced minima cause rapid development of planar facets of large extent. When the minimum can be treated as a small perturbation, the extent of the corresponding facet becomes very limited.

3. Curved portions of the etched sections of a cylindrical hollow are formed around the minima in **L**. Conversely, elements whose orientation are in the

vicinity of an orientation associated with a maxima in **L** contribute to the curved, etched regions of an initially circular crystal. These contributions to the etched sections arise when the extremum under consideration lies between two extrema of different nature and slight amplitude (see for example the formation of the curved portions in Figs 4c and 5c due to the respective minimum m_3 and maximum M_4). All these conclusions corroborate the proposed theorems.

3. Applications to combined etching and lithography techniques

This section includes the theoretical results required for a correct prediction of the geometrical features of dissolution shapes obtained by anisotropic chemical photolithographic processes.

3.1. Dissolution cross-sectional profiles at a mask edge

For an etched linear stripe the elements forming the sides of the etched cross-section are only composed of concave intersections; therefore in the following we are only concerned with theorem 1 (see Section 2). The unmasked surface dissolves at a constant slowness and remains parallel to the initial flat surface. Under the inert mask, the etched profile can be characterized by the extent of the underetch U corresponding to the distance OU (Fig. 6) and by the angle γ which is the angle of the bordering etch plane (or bordering element) to the wafer surface. In practical applications such as micromachining, a precise knowledge of U and γ is highly desirable.

3.1.1. Etched sections and polar graphs

In this section we specify the role played by extrema of the dissolution slowness in the development of curved portions and in the faceting of the etched cross-sectional profile. Firstly, we work with various polar graphs corresponding to singly rotated planes, and secondly for a given polar graph we change the portion of the graph involved in the theoretical simulation. Fig. 6 includes a brief description of the geometry, but some explanatory comments are needed. The direction of the normal $\mathbf{n}_a$ to the plane $(0zy')$ coincides with the x' axis related to the singly rotated slice $(0x'z')$ of orientation $\varphi = \varphi_0$, $\theta = 0°$, and we assume that the original slice to be etched corresponds to the plane $(0x'y')$, i.e. to the plane $(0xy)$. The successive etched slices are then obtained by rotating the original slice of an angle α about the normal $\mathbf{n}_a$. It is obvious that the etched section at the mask edge is composed of elements whose orientations are detected by means of an angle β^* (Fig. 6c) lying in the range (90–270°). In this condition, as α varies we have only to consider different portions of the polar graph obtained by fixing to φ_0 the value of the angle of cut, φ, to construct geometrically the successive theoretical cross-sections. To permit an extensive investigation, more and more complicated polar graphs are studied and for a given polar graph the successive etched slices have orientations for which the dissolution slowness passes crudely through an extremum. Applying simply theorem 1 (Section 2) we obtain the predicted cross-sectional morphologies of Tables I–III which are

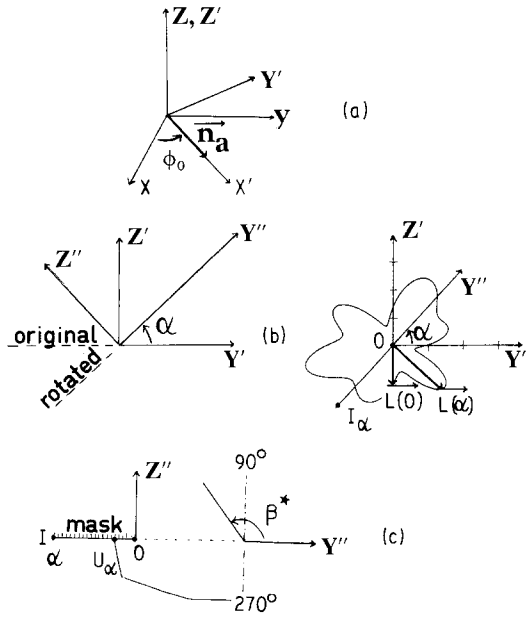

Figure 6 Localized etching on differently oriented slices. (a) Geometry of slices; (b) polar diagram and orientation of the inert mask of extent OI_α; (c) cross-sectional view of the etched profile and geometrical parameters involved in the numerical simulation.

TABLE I Etched cross-sectional profiles as obtained from simplified geometrical constructions, where $\varphi_0 = 60°$ and $N_{max} = 4$. The inward normal, n_0, to the etched surface lies parallel to OM_i or Om_i

Extremum: M_i or m_i	α	Etched section
M_1	0°	
m_1	55°	
M_2	125°	
m_2	180°	

TABLE II Etched cross-sectional profiles as obtained from geometrical constructions where $\varphi_0 = 60°$ and $N_{max} = 6$.

Extremum: M_i or m_i	α	Etched section
M_1	0°	
m_1	55°	*
M_2	117°	
m_2	145°	
M_3	180°	

* Scales divided by two.

based on the polar diagrams displayed in Fig. 5a, b and d of Part I [21]. To draw these profiles we suppose that the two successive facets are never joined together by a rounded portion corresponding to converging trajectories associated with minima m_i of the dissolution slowness, even when the etched slice has a minimum slowness.

TABLE III Etched cross-sectional profiles as obtained from geometrical constructions where $\varphi_0 = 60°$ and $N_{max} = 10$

Extremum: M_i or m_i	α	Etched section
M_1	0°	
m_1	35°	*
M_2	55°	*
m_2	80°	*
M_3	117°	
m_3	145°	
M_4	180°	

*Scales divided by two.

The graphical simulation gives more details. In the following, to avoid confusion, the etched reference surface is designated by means of its angle of rotation α, and by means of its dissolution slowness vector which lies parallel to the inward normal **n** to the surface. The inert mask is located in $I_\alpha O$ where O is the origin of the polar diagram (Fig. 6). Starting with the polar graph of Fig. 5a of Part I [21] and with reference surfaces lying perpendicular to OM_1, Om_1, OM_2 and Om_2, we obtain the respective cross-sectional profiles of Fig. 7a–d. We observe that in several cases we obtain curved facets rather than the planar facets expected theorem 1 (Section 2). This may be interpreted in terms of small maxima in **L** with respect to the value of the minimum dissolution slowness at m_2. Effectively, the limiting facets associated with the maxima M'_2 and M_2 do not appear in the respective cross-sectional profiles of Fig. 7a and d. But examination of Fig. 7b and d reveals also that the respective minima m_1 and m_2 contribute to the rounded portions bc of these dissolution profiles. Introducing for $N_{max} = 6$ (Fig. 5b, Part I [21]) a minimum m_1 of greater amplitude gives rise to a rounded region whose extent seems of more importance (Fig. 8b). Moreover changing the small perturbation m_2 in Fig. 5a (Part I [21]) by a small perturbation, M_2 of different nature (Fig. 5a,

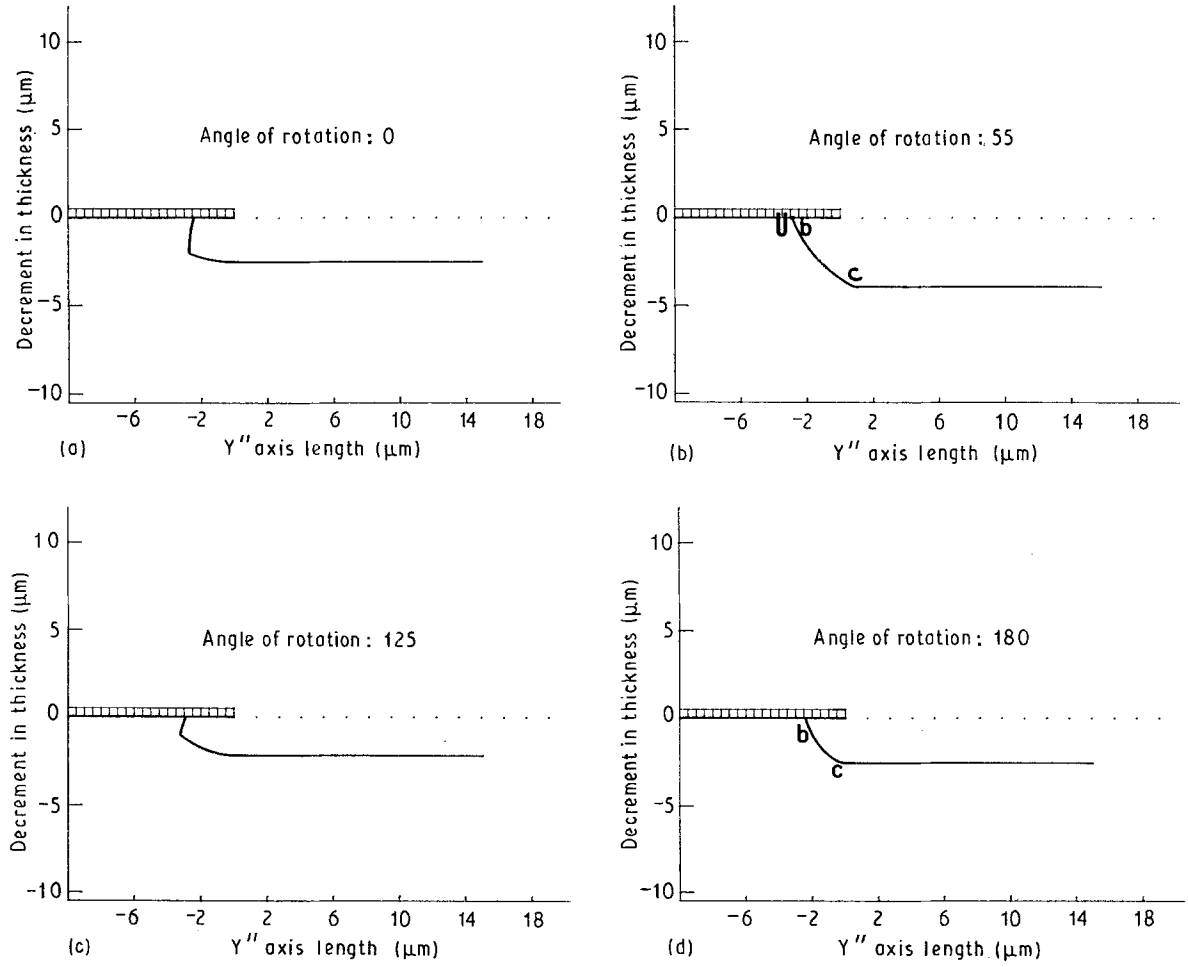

Figure 7 Theoretical cross-sectional profiles for differently oriented slices whose dissolution slowness vector coincides (Fig. 5a, Part I [21]) with (a) $\mathbf{OM}_1$ (b) $\mathbf{Om}_1$ (c) $\mathbf{OM}_2$ and (d) $\mathbf{Om}_2$. $N_{max} = 4$, $\varphi_0 = 60°$.

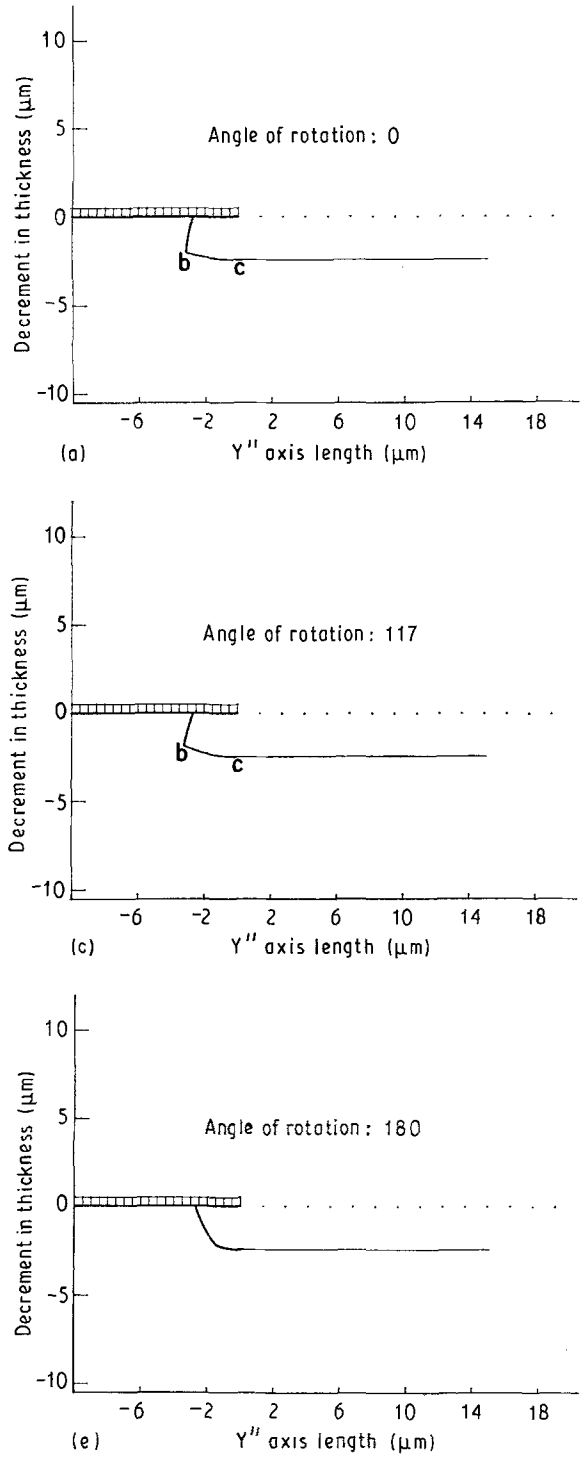

Figure 8 Theoretical cross-sectional profiles for various slices whose dissolution slowness vector coincides (Fig. 5b, Part I [21]) with (a) $\mathbf{OM}_1$, (b) $\mathbf{Om}_1$, (c) $\mathbf{OM}_2$, (d) $\mathbf{Om}_2$ and (e) $\mathbf{OM}_3$. $N_{max} = 6$, and $\varphi'_0 = 60°$.

Part I [21]) does not modify significantly the shape of the etched profile if the orientation of the reference surface corresponds to that of the small perturbation (compare Figs 7d and 8e). The curved portions b c in Fig. 8a and c can be understood in terms of the diverging trajectories of elements whose dissolution slowness lies in the respective vicinity of P'_1 and P_1. These observations are corroborated by the results derived for $\varphi_0 = 60°$ and $N_{max} = 10$ (Fig. 5d, Part I [21]). The cross-sectional profiles displayed in Fig 9a–h allow us to draw the following conclusions.

1. The maxima in **L** contribute to all the faceted portions of the dissolution cross-sectional profiles.

2. Flat regions tend to intersect to form a distinct obtuse or acute angle, provided a pronounced minimum lies between two successive sharp maxima (Fig. 9d and f).

3. Even a minor maximum in **L** (M_4 in Fig. 5d, Part I [21]) causes the development of an intermediate facet b c (Fig. 15h) if the relative amplitudes of the extrema involved in the simulation remain of comparable importance. This point has previously been made by Shaw [14, 15].

4. The shape of the etched profile enlarges but does not change with repeated etchings, as evinced by Fig. 9h. This remark agrees well with previous observations by Shaw [14, 15] who noticed that the basic cross-sectional profile will be independent of the extent of etching, as confirmed by experiments.

5. The relative apparent extent U_a of the crudely planar facet associated with the maximum M_1 in Fig. 5d (Part I [21]) is more accentuated when the reference surface coincides with a maximum of **L** (Figs 9c and e) than with a minimum (Fig. 9b).

6. In Fig. 9e, the slightly curved portion a b can be attributed to diverging trajectories associated with elements whose orientation is in the range (P_2–M_3). These elements mask the slight contribution of the maximum M_2 to the etched profile. Similar behaviour is observed in Fig. 9a.

All these remarks show the complexity of the anisotropic dissolution process, and explain why the approx-

imate geometrical construction fails in some cases to derive the exact theoretical cross-sectional profiles.

3.1.2. Underetch U and bordering angle γ

For the fabrication of micromechanical devices by combined selective anisotropic etching and lithography techniques, it is interesting to present some quantitative results which characterize the anisotropy of a given etchant system: on the one hand, the angle γ related to the etch-bordering element that develops during the chemical attack and sometimes coincides with a limiting facet, and on the other hand, the extent of the underetch U. Of course for the geometrical constructions displayed in Tables I–III the theoretical value of the bordering angle γ is directly connected to the orientation of the profile element, for which the dissolution slowness passes through a maximum. But because of the complexity of the anisotropic dissolution, the numerical values of the angle γ, as computed from the graphical simulation (Table IV) by evaluating the slope of the profile element just beneath the inert mask, deviate more and less from the preceding theoretical values. These discrepancies can be understood in terms of the important role played by the diverging trajectories in the formation of the bordering profile element.

Another important characteristic feature of the anisotropy is the underetch U, represented by the distance OU_α in Figs 7 to 9. For the etched slices which are obtained by rotating the reference slice of $\alpha°$ about the x' axis, it appears that the polar U against α plot can be graphically determined using the program for the numerical simulation of the dissolution shapes of cylindrical hollow. We have just to store a zero value for the radius of the starting circular section. The results displayed in Fig. 10 for the three cases studied in Section 3.1.1. indicate clearly that the underetch presents minima for the orientations corresponding to maxima of the dissolution slowness. At this point, it should be noted that the polar plots of Fig. 10 can also be conveniently used to draw with a relatively good approximation the dissolution cross-sectional profiles related to the differently oriented slices.

TABLE IV Values of the bordering angle, γ, as estimated from geometrical constructions (γ_G) and as computed (γ_N). The inward normal n_0 to the etched surface lies parallel to OM_i or Om_i.

$\varphi_0 = 60°$, $N_{max} = 10$ Extremum: M_i or m_i	γ_G (deg)	γ_N (deg)
M_1	117	114
m_1	35	41
M_2	55	58
m_2	80	81
M_3	117	114
m_3	153	138
M_4	63	66
m_3'	90	95
$\varphi_0 = 60°$, $N_{max} = 6$ Extremum	γ_G	γ_N
M_1	117	109
m_1	55	62
M_2	117	114
m_2	145	132
M_3	63	71
$\varphi_0 = 60°$, $N_{max} = 4$ Extremum	γ_G	γ_N
M_1	125	108
m_1	55	67
M_2	125	108
m_2	55	72

3.2. Characterization of star-like structures

To determine which etchant system is more appropriate for given specific applications in micromechanics, it is necessary to determine the orientation dependence of the etch rate, i.e. of the dissolution slowness. To avoid the necessity to evaluate the normal etch rate of a great number of differently, oriented slices, some authors [23, 24] have suggested using a star-shaped mask with a small angular distance, β, between the segments to pattern the wafer. The interest in such a structure comes from the fact that the lateral underetch, U_L, is transformed into a radial direction. Then for a slice with any orientation we measure a radial underetch, U_R, which in reality constitutes an average amplified image of the two different lateral underetches U_{L1} and U_{L2} associated with a segment of the star (Fig. 11). Few experiments on star-like structures have been reported in the literature [24–26]. Moreover, all these works have been performed on $\langle 1\,0\,0\rangle$ and $\langle 1\,1\,0\rangle$ oriented wafers of silicon, a material with a relatively high degree of symmetry. Therefore it is of interest to undertake a more systematic theoretical study of star-like structures patterned on non-centrosymmetric crystals. For this purpose the changes in U_R with the orientation Ψ, of a segment are numerically computed starting from various singly rotated slices. Since the star mask is composed of successive segments whose orientations are defined by an angle, Ψ lies on a singly rotated slice with $\varphi = \varphi_0$ and $\theta = 0°$. The two cross-sectional profiles lying in plane $(0\,y''\,z'')$ are associated with a direction x'', making an angle $\Psi \pm \beta/4$ with the direction x'. In these conditions, all the elements which are incorporated in the final dissolution profile are generally connected to doubly-rotated surface elements. Thus a display of computed results can be accomplished provided the angles Ψ and θ, associated with any potentially present element of the cross-sectional profile, were precisely evaluated. The program includes two essential steps. Firstly, as required for the solution, the computer provides the two cross-sectional profiles related to the two directions x'' defined by the angles $\Psi + \beta/4$ and $\Psi - \beta/4$, and then calculates the lateral underetches U_{L1} and U_{L2}. Secondly, geometrical arguments are used to compute the average underetch U_R as a function of the angle Ψ. The program takes a relatively long time (about 1 h) to execute the first step, in which for the two cross-sectional profiles a great number of elements with converging trajectories must be eliminated. Then to reduce the total time of calculation we have chosen on the one hand to work with

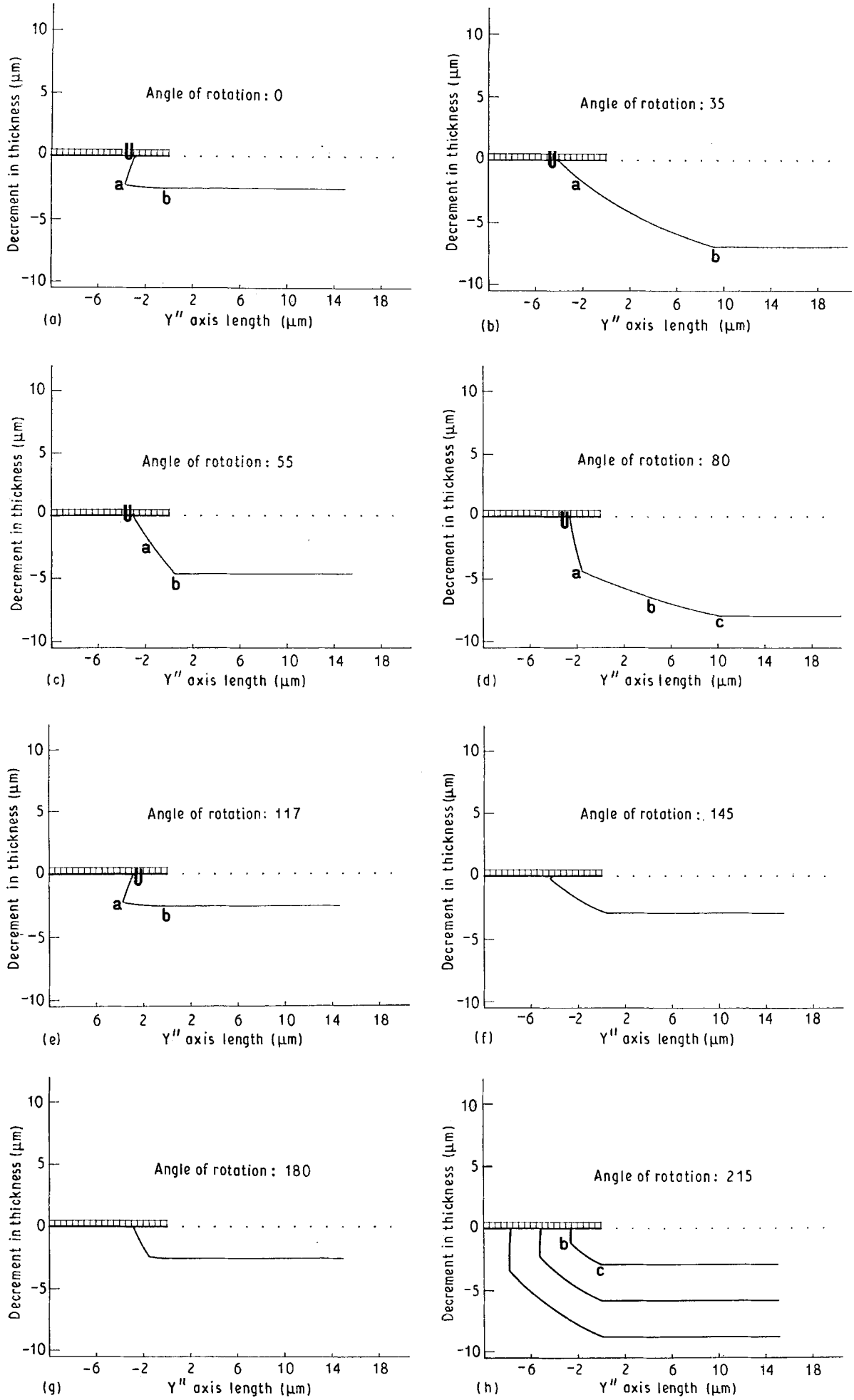

Figure 9 Theoretical cross-sectional profiles for various slices whose dissolution slowness vector coincides (Fig. 5d, Part I [21]) with (a) $\mathbf{OM}_1$, (b) $\mathbf{Om}_1$, (c) $\mathbf{OM}_2$, (d) $\mathbf{Om}_2$, (e) $\mathbf{OM}_3$, (f) $\mathbf{Om}_3$, (g) $\mathbf{OM}_4$ and (h) $\mathbf{Om}'_3$. $N_{max} = 10$, $\varphi_0 = 60°$.

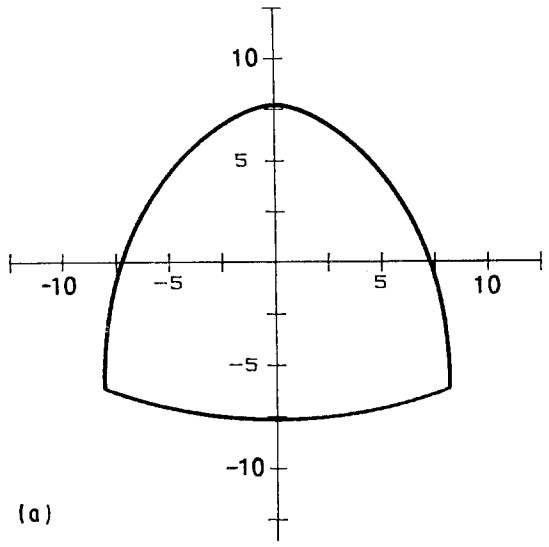

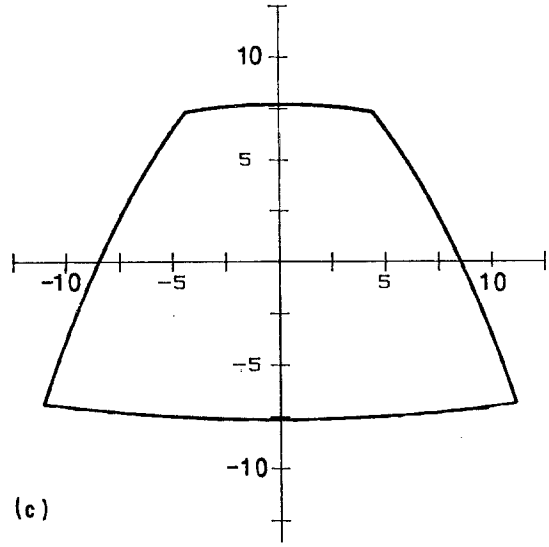

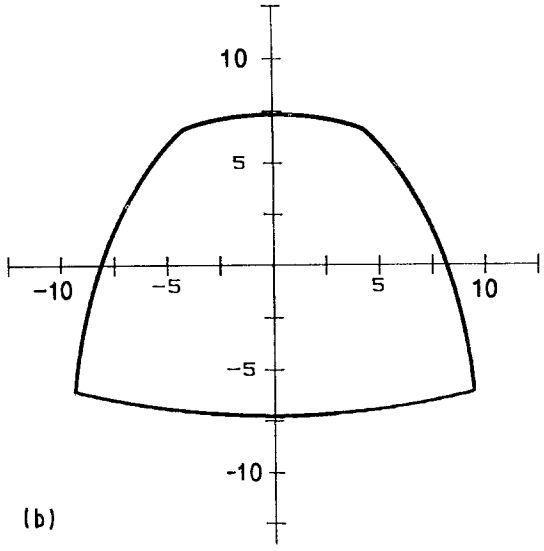

Figure 10 Changes in the underetch U with the angle of rotation α as given by numerical simulations starting with various polar diagrams. (a) $N_{max} = 4$, $\varphi_0 = 60°$; (b) $N_{max} = 6$, $\varphi_0 = 60°$; (c) $N_{max} = 10$, $\varphi_0 = 60°$.

initial profiles composed of successive elements whose orientation changes from degree to degree, and on the other hand to enter the value of two degrees for the input variable β, in order to repeat the procedure only 180 times.

The theoretical U_R against Ψ polar plots as computed for $\Psi_0 = 0°$, 45° and 60° are displayed in Fig. 12a–c, respectively. These figures merit some comments.

Firstly, the curve related to $\varphi_0 = 60°$ presents for Ψ around 50° and 230° a somewhat oscillatory behaviour. This behaviour may be attributed to slight numerical inaccuracies in the computation. Effectively, discrepancies between the calculated values of U_{L1} and U_{L2} and the exact values can appear when the trajectories of elements in the vicinity of the true bordering element markedly diverge, so that for successive orientations that differ from one degree, the distance between two points forming the etched profile can become important. In these conditions a truncation error can occur and an intersection I beneath the mask similar to that appearing in Fig. 9f can be accidentally masked. To avoid this difficulty, we can divide by ten the interval of variation, δ_A, for successive angles, but after such a modification the program will take a long time to execute and we have decided to keep δ_A unchanged.

For $\varphi_0 = 0°$ the U_R against Ψ polar plot satisfies the twofold symmetry characteristic of the (1 0 0) crystal. However the polar plots related to $\varphi_0 = 45°$ (Fig. 12b) and $\varphi_0 = 60°$ (Fig. 12c) are apparently symmetrical about the vertical and horizontal axes; such an observation cannot be simply understood in terms of the

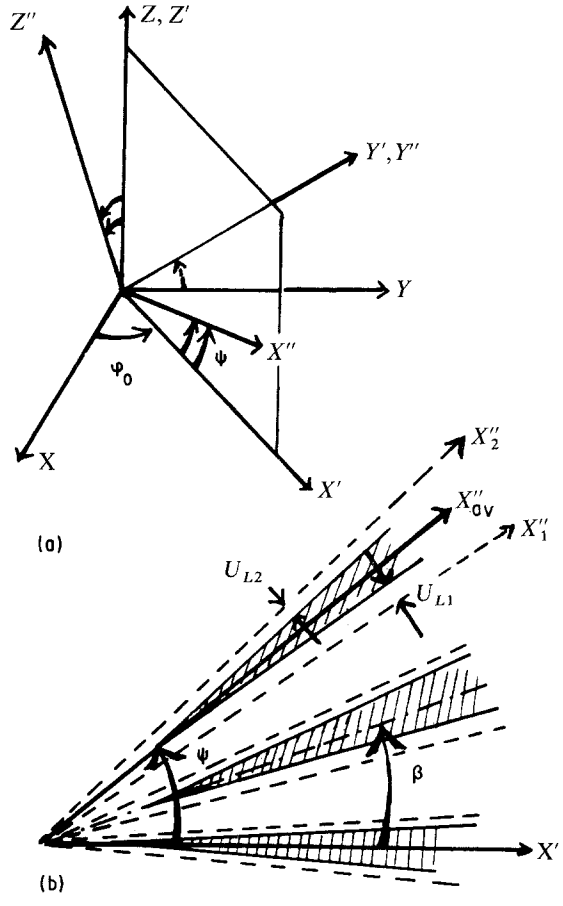

Figure 11 The geometry of a star-like structure.

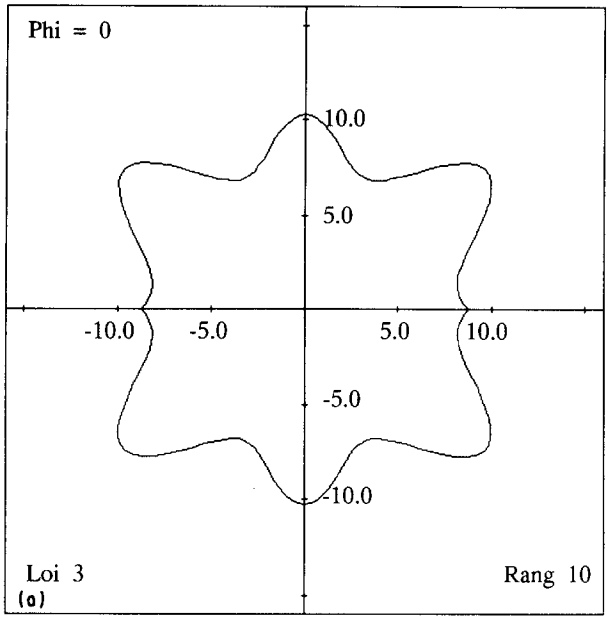

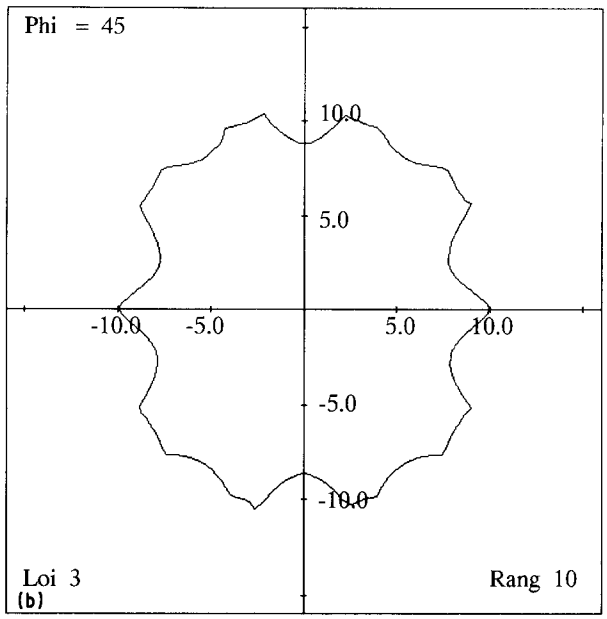

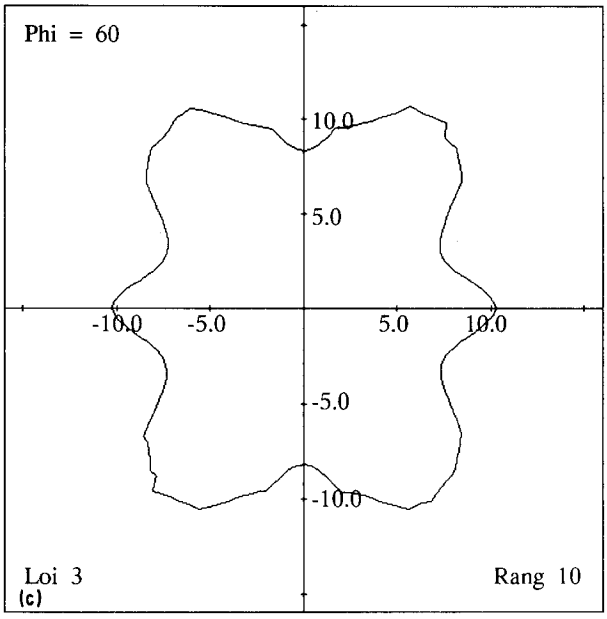

Figure 12 Theoretical polar plots of the radial underetch for a star-shaped mask patterned on various singly-rotated wafers. (a) $\varphi_0 = 0°, \theta_0 = 0°$; (b) $\varphi_0 = 45°, \theta_0 = 0°$; (c) $\varphi_0 = 60°, \theta_0 = 0°$. The plots are computed for $N_{max} = 10$.

symmetry of the cubic point group 23. Thus in addition, polar graphs of the dissolution slowness are given (Figs 13 and 14c) for $\varphi_0 = 45°$ and for a rotation angle Ψ equal to Ψ_0, $180 - \Psi_0$ and $\Psi = 180 + \Psi_0$, respectively. It is sufficient to invert Fig. 14c to obtain the polar diagram displayed in Fig. 13a. Such a result can be understood by remembering that the axis z′ is identified with the twofold axis [0 0 1], and that the two polar graphs of the dissolution slowness are just those contained in the two cross-sectional planes transformed under operation 2, then the general shape of the polar graph will remain invariant. Comparing Fig. 13a and b, it is obvious that we are concerned with the same cross-sectional plane. It is therefore not surprising that the polar plot of Fig. 13b can be considered as the mirror image of the polar plot of Fig. 13a. When evaluating the two lateral underetches U_{L1} and U_{L2}, we can for the sake of simplicity consider that we start with an average single polar corresponding to Ψ_0. In this condition, to compute U_{L2} we need a region of the original polar graph which is just an

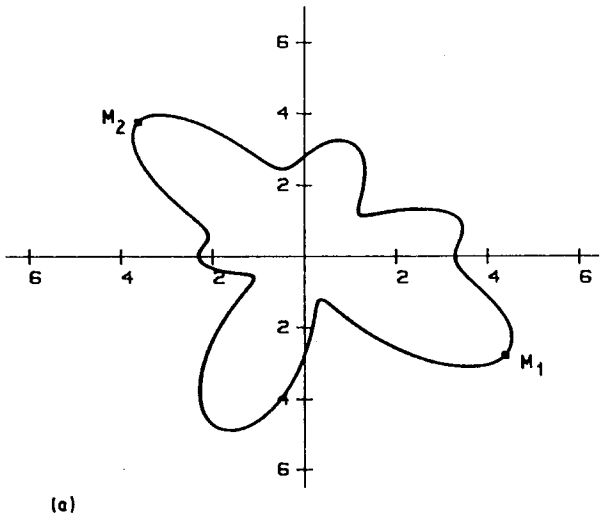

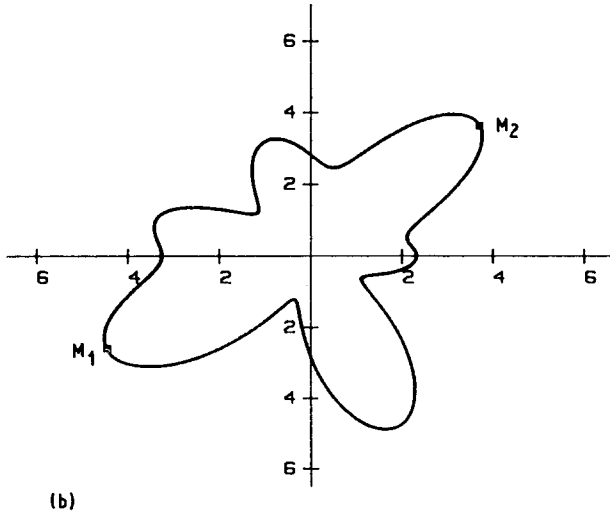

Figure 13 Polar diagrams of the dissolution slowness as involved in the numerical simulation when $\varphi_0 = 45°$ and (a) $\Psi = \Psi_0 = 56°$, $N_{max} = 10$; (b) $\Psi = \Psi_0 + 180°$, $N_{max} = 10$.

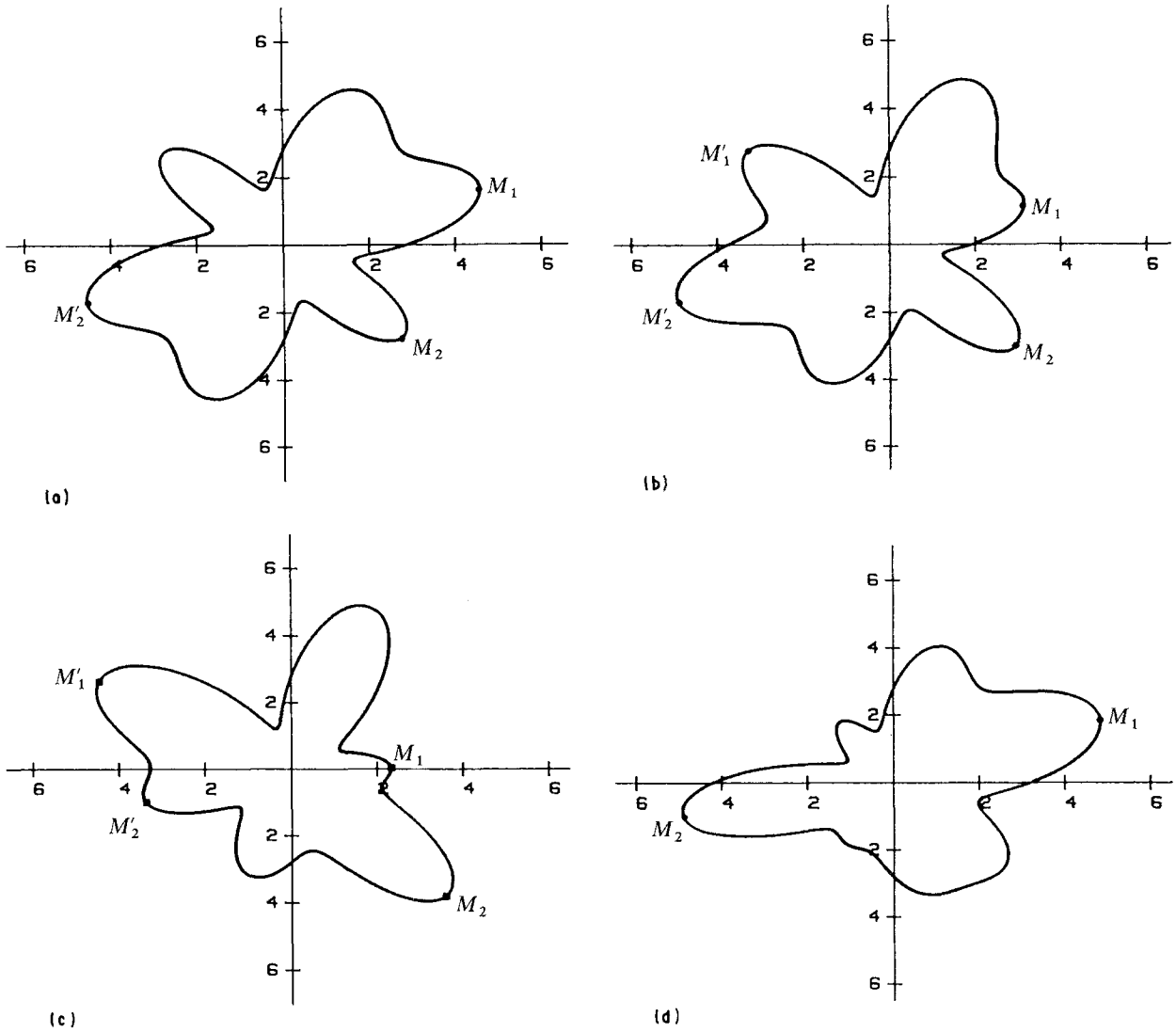

Figure 14 Polar diagrams of the dissolution slowness as involved in the numerical simulation when $\varphi_0 = 45°$ and (a) $\Psi_0 = 90°$, $N_{max} = 10$; (b) $\Psi_0 = 102°$, $N_{max} = 10$; (c) $\Psi_0 = 124°$, $N_{max} = 10$; (d) $\Psi_0 = 164°$, $N_{max} = 10$.

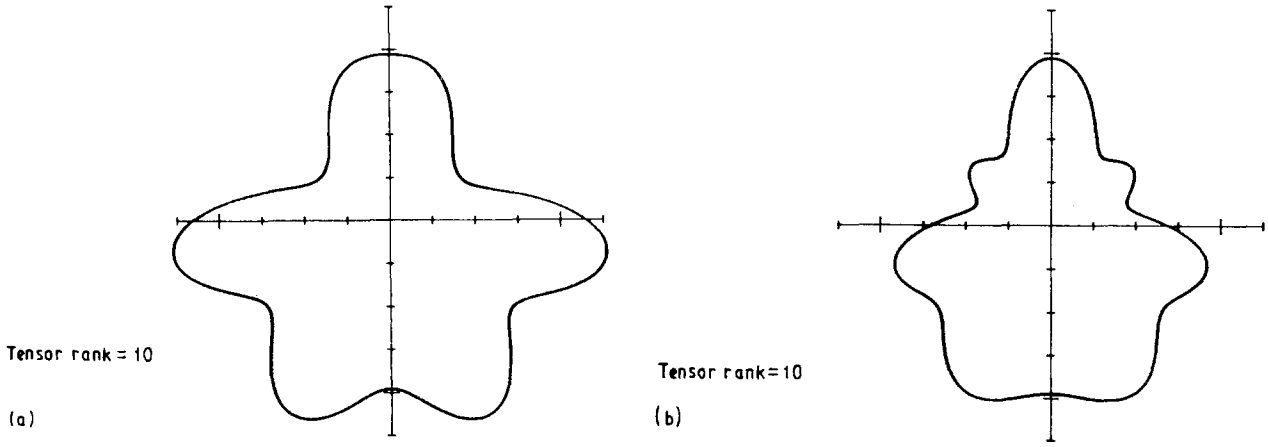

Figure 15 Polar diagrams of the dissolution slowness corresponding to (a) $\varphi_0 = 150°$; (b) $\varphi_0 = 135°$.

inversion (180° rotation) of the polar diagram yielding U_{L1}. Since for the polar plot shown in Fig. 14c U_{L1} and U_{L2} are correlated to the accentuated maxima M_2 and M'_1, it is left as an exercise for the reader to show from rapid geometrical constructions that in the case where $\Psi = \Psi_0$ and $\Psi = 180 + \Psi_0$ the same maxima M_2 and M'_1 are also to be accounted for the estimation of U_{L1} and U_{L2}. From this argument we can conclude that the radial underetch U_R remains unchanged when the rotation angle Ψ takes values respectively equal to Ψ_0, $180° - \Psi_0$ and $\Psi_0 + 180°$, leading to the apparent symmetrical situation observed in Fig. 12b and c.

It is obvious that the final etched shape of a star-like structure patterned on a slice of orientation φ_0, $\theta = 0°$, is not simply connected to the shape of the polar graph L $(\varphi_0 + 90°, \theta)$ located in a plane of similar orientation (see for example Fig. 15a and b). As

a consequence models that use the etched shapes of differently oriented star-like structures to estimate the shape of the corresponding polar plots and by extension the shape of the dissolution slowness surface do not appear as easily workable.

To discuss, for various values of the angle of cut φ_0, the etched shapes of the star-like structure we have to examine the polar graphs associated with different values Ψ_0 of the rotation angle Ψ. For a rapid analysis, geometrical constructions can be conveniently performed to yield the approximate etched shape of the cross-sectional profiles and to predict which maxima are responsible for the formation of bordering facets. Here we have chosen to restrict our analysis to values Ψ_0 of the rotation angle associated with minima and maxima in the radial underetch U_R. For this purpose we undertake a systematic examination of the polar graphs illustrated in Figs 14, 16 and 17.

Starting with a slice of orientation $\varphi_0 = 0°$, we can easily show that the minima in U_R which occur for Ψ_0 around 116° and 172° are determined by the two accentuated maxima M_2 and M'_2 in the dissolution slowness (Fig. 16b and d). Moreover, the maxima in U_R observed for $\Psi_0 = 90°$ and $\Psi_0 \approx 144°$ are directly connected to the development of bordering facets associated with the less accentuated maxima M_2 and M'_2 as indicated respectively in Fig. 16a and c. We can infer that whatever the value of φ_0, the minima in U_R are produced for particular values of Ψ for which maxima of large amplitude in the polar graph $\mathbf{L}$ (φ_0, Ψ_0) contribute to the development of the bordering facets. Conversely maxima in U_R are correlated to relatively minor maxima in $\mathbf{L}(\varphi_0, \Psi_0)$. To verify this statement, consider the case where $\varphi_0 = 45°$ (Fig. 14). For $\Psi_0 = 90°$, the minimum in U_R can be attributed to the maxima M_1 and M'_2 in Fig. 14a. As Ψ_0 changes from 90° to 102° (Fig. 14b) the amplitude of the maximum M_1 which contributes to the lateral etch decreases and U_R passes through a maximum. As Ψ_0 takes a value of 124° (Fig. 14c), the bordering facets are again associated with major maxima and U_R falls to a relative minimum (Fig. 12b). Moreover, the sharp minimum in U_R appearing for Ψ_0 around 164° can be understood in terms of the maxima of largest amplitude M_2 and M'_2 in Fig. 14d. For $\varphi_0 = 60°$, similar treatment can be given to explain the maximum and the minimum in U_R occurring for $\Psi_0 = 124°$ and $\Psi_0 = 160°$, respectively. The minimum in U_R is obviously due to the two large maxima M_1 and M'_2 in the polar graph of Fig. 17b, whereas the maximum in U_R

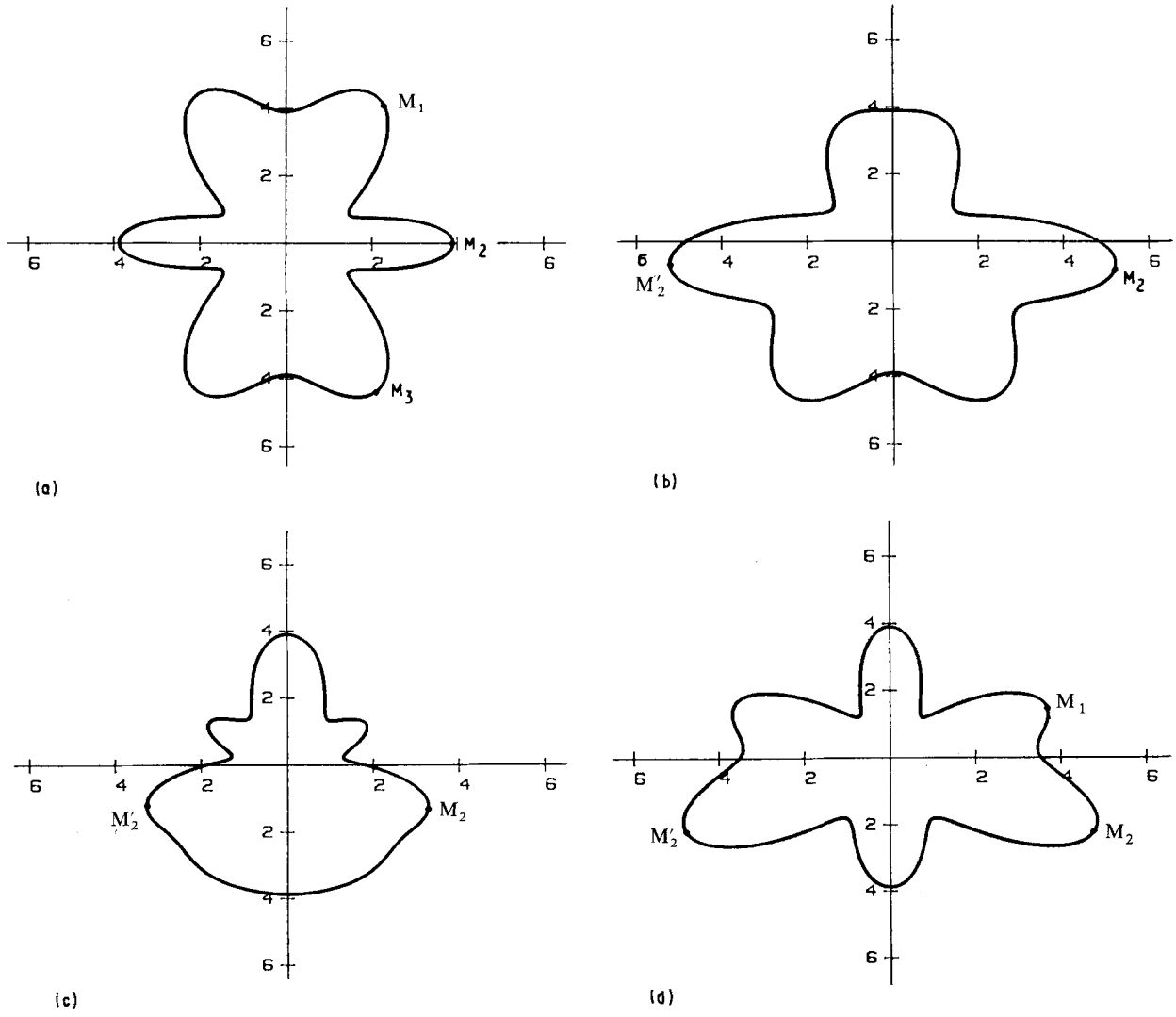

Figure 16 Polar diagrams of the dissolution slowness as involved in the numerical simulation when $\varphi_0 = 0°$ and (a) $\Psi_0 = 90°$, $N_{max} = 10$; (b) $\Psi_0 = 116°$, $N_{max} = 10$; (c) $\Psi_0 = 144°$, $N_{max} = 10$; (d) $\Psi_0 = 172°$, $N_{max} = 10$.

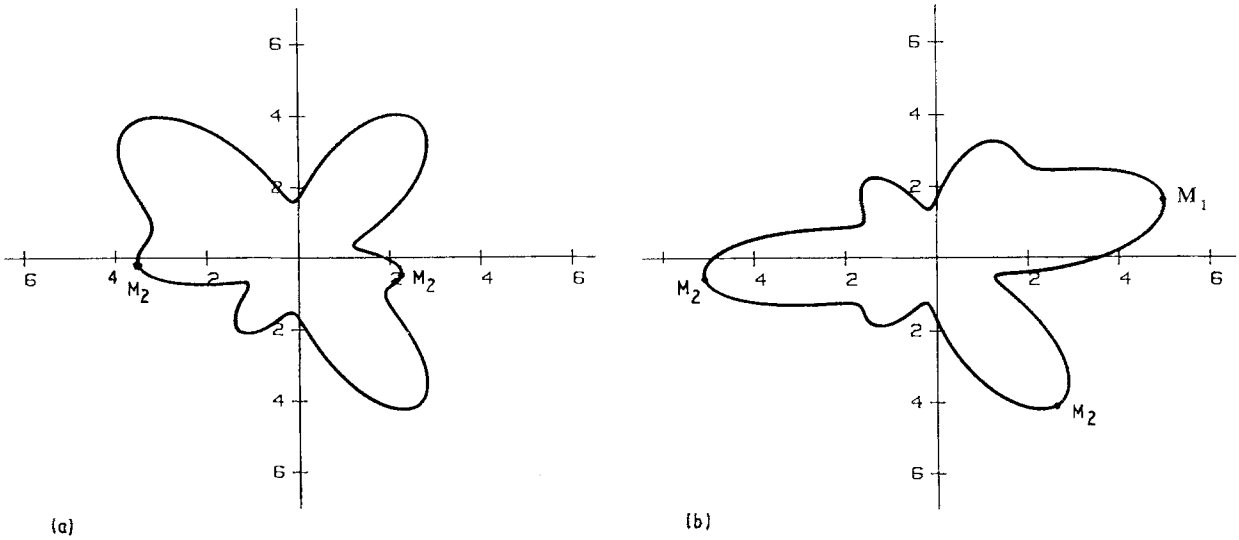

Figure 17 Polar diagrams of the dissolution slowness as involved in the numerical simulation when $\varphi_0 = 60°$ and (a) $\Psi_0 = 124°$, $N_{max} = 10$; (b) $\Psi_0 = 160°$.

results from the relatively minor maximum M_2 in $\mathbf{L}(\varphi_0, \Psi_0)$ (Fig. 17a).

4. Conclusion

Numerical procedures have been derived to represent graphically the etched shapes of crystals with simple starting shapes on the one hand, and on the other, the cross-sectional dissolution profiles resulting from localized etching at the edge of an inert mask. These procedures have been compared with theoretical geometrical constructions based on Wulff's procedure. These comparisons show without ambiguity that the graphical simulation gives etched profiles with more precise geometrical features. Moreover, the important role played by diverging trajectories associated with elements in the vicinity of limiting facet elements in forming the final etched profile is clearly outlined.

Quantitative information on technical problems caused principally by underetching can be also extracted from these numerical procedures, in particular the changes in the extent of underetching and in the value of the bordering angle with orientation can easily be evaluated numerically. In addition, theoretical etched shapes of star-like etching patterns can be also drawn using the graphical simulation involving the equation of slowness surface. All this precise information is necessary when a choice of orientation is required to minimize, for example, the lateral etch.

References

1. H. C. GATOS and M. C. LAVINE, *J. Electrochem. Soc.* **107** (1960) 427.
2. R. B. HEIMANN, in "Silicon Chemical Etching", edited by J. Grabmaier (Springer, Berlin, 1982).
3. M. W. WEGNER and J. M. CHRISTIE, *Phys. Chem. Minerals* **9** (1983) 67.
4. C. R. TELLIER, *Surf. Technol.* **21** (1984) 83.
5. H. C. GATOS and M. C. LAVINE, *J. Electrochim. Soc.* **107** (1960) 433.
6. M. CASTAGLIOLA, C. R. TELLIER and J. L. VATERKOWSKI, *J. Mater. Sci.* **21** (1986) 3551.
7. R. J. JACCODINE, *J. Appl. Phys.* **33** (1962) 2643.
8. F. C. FRANK and M. B. IVES, *ibid.* **31** (1960) 1996.
9. B. W. BATTERMAN, *ibid.* **28** (1957) 1236.
10. B. A. IRVING in "The Electrochemistry of Semiconductors", edited by P. J. Holmes (Academic, London, 1962) p. 256.
11. K. SANGWAL, "Etching of Crystals" (North-Holland, Amsterdam, 1987).
12. M. LIGHTHILL and G. WHITMAN, *Proc. Roy. Soc. A* **229** (1955) 281.
13. F. C. FRANK, in "Growth and Perfection of Crystals", edited by R. H. Doremus, B. W. Robert and D. Turnbull (Wiley, New York, 1958) p. 411.
14. D. W. SHAW, *J. Electrochem. Soc.* **128** (1981) 874.
15. D. W. SHAW, *J.Crystal Growth* **47** (1979) 509.
16. G. WULFF, *Z. Krist.* **34** (1901) 449.
17. C. R. TELLIER, N. VIALLE, J. L. VATERKOWSKI, in Proceedings of the 40th Annual Symposium on Frequency Control, Philadelphia, Pennsylvania, 1986 (IEEE, New York, 1986) p. 76.
18. C. R. TELLIER and J. L. VATERKOWSKI, *J. Mater. Sci.* **24** (1989) 1077.
19. C. R. TELLIER and T. G. LEBLOIS, in Proceedings of the Third European Time and Frequency Forum, Besancon, France, 1989 (Imprimerie de Conseil General du Doubs) pp. 246–255.
20. C. R. TELLIER, *J. Cryst. Growth* **700** (1990) 515.
21. A. BRAHIM-BOUNAB, J. Y. AMAUDRUT and C. R. TELLIER, *J. Mater. Sci.* (in press).
22. C. R. TELLIER, *J. Cryst. Growth* **96** (1989) 450.
23. G. DELAPIERRE, *Sensors and Actuators* **17** (1989) 123.
24. H. SEIDEL and L. CSEPREGI, *ibid.* **4** (1983) 455.
25. U. SCHNAKENBERG, W. BENECKE and B. LOCHEL, *ibid.* **A23** (1990) 1031.
26. L. CSEPREGI, *Microelectr. Engng* **3** (1985) 221.

Received 18 June
and accepted 19 October 1990